UV durability assessment of a thermoplastic epoxy-based hybrid composite rod for structural reinforcement and retrofitting

Jonathon Tanks[a*], Kimiyoshi Naito[a,b]

[a] National Institute for Materials Science, Research Center for Structural Materials, 1-2-1 Sengen, Tsukuba, Ibaraki, Japan 305-0047

[b] Tohoku University, Department of Aerospace Engineering, 6-6-1 Aramaki-aza-Aoba, Aoba-ku, Sendai, Miyagi, Japan 305-0047

* Corresponding author

Tel: +81-29-859-2606

Fax: +81-29-859-2401

E-mail address: TANKS.Jonathon@nims.go.jp

Abstract

Recently, a hybrid composite cable has been developed for external strengthening of structures in seismically active zones, containing a novel thermoplastic epoxy matrix. While this resin has advantageous properties such as processability, the UV resistance for outdoor service conditions has not been studied. This paper examines the accelerated UV degradation behavior by using a xenon arc source, and reporting the changes in chemical structure and mechanical properties of both the resin and FRP rods. While the neat resin is susceptible to photo-oxidation and a sharp decline in strength, the hybrid FRP shows no significant changes in tensile properties even after nearly 2000 MJ/m^2 of UV radiation (equivalent to seven years in Florida, USA). This was attributed to the fiber-dominant nature of unidirectional composites, further supported by a Curtin-type analytical model.

Keywords: thermoplastic epoxy; accelerated weathering; hybrid FRP; UV resistance.

1. Introduction

Infrastructure such as bridges, tunnels, marine structures, nuclear plants, and railways, as well as industrial and commercial infrastructure such as warehouses and office buildings, are vital to commerce and social prosperity. While steel frame structures are commonly found in office buildings and roadway bridges, reinforced and prestressed concrete remains the most common system in the world [1]. However, corrosion of the steel reinforcing/prestressing materials—usually bars or cables—leads to cracking of the concrete and costly repairs over the life of the structure [1-3]. Of the various alternative materials and preventative measures available, fiber reinforced polymer (FRP) composites have steadily attracted attention in the infrastructure sector as a new concrete reinforcement material, due to their excellent strength-to-weight ratio and insusceptibility to galvanic corrosion [4-8]. In addition to internal reinforcement (i.e., inside the concrete), where water- and alkali-resistance is essential, external reinforcement applications have also been investigated. In particular, lightweight FRP is an ideal material for seismic retrofitting of in-service concrete and steel structures, since less inertia is generated by high-frequency vibrations [9,10].

However, these polymeric composites are susceptible to environmental degradation, which includes a vast range of mechanisms and rates depending on the specific polymer

and the environmental conditions; numerous studies have reported on neat polymer and FRP degradation in aqueous solutions of various pH and temperature to simulate a concrete environment [11-15]. While this is applicable for internal reinforcement, external applications involve exposure to sunlight—particularly damaging UV radiation [16-18]. Since epoxy-based resins are widely used as FRP matrix materials, UV degradation of thermoset epoxy and its FRP has been well studied [19-27]. A thermoplastic polymer known as phenoxy, having a similar chemical formula to many bisphenol-based thermoset epoxies, has been used in numerous photo-degradation studies as a model polymer [28-31]. Previous work found that tertiary carbons in the phenoxy chain are attacked in the form of α- and β-scission, while secondary carbons are oxidized to ketones and followed by photo-Fries rearrangement (phenol hydroxylation) [20,24,29-35].

Recently, a glass/carbon hybrid fiber reinforced composite cable (Figure 1a), using a novel phenoxy-based thermoplastic epoxy matrix, was developed for external seismic retrofitting of structures (CABKOMA, Komatsu Matere Co., Ltd.) [9,36]. The stranded cable is composed of seven hybrid rods, comprised of a carbon fiber core and a braided glass fiber outer sheath, and is available in three sizes depending on the carbon fiber content—NH2417 (one 24K tow), NH2427 (two 24K tows), and NH2437 (three 24K

tows), having cable diameters of 7.0 mm, 8.2 mm, and 9.3 mm, respectively [9]. In addition to exhibiting a hybrid effect on the tensile, flexural and compressive properties under static and fatigue loading [36-42], this cable structure also provides electrical insulation to prevent galvanic corrosion in cases where contact with metal components is unavoidable.

Although the mechanical properties of the composite cable without aging have been investigated [36-42], the UV resistance of the rods and its thermoplastic epoxy has not. This paper reports the accelerated UV degradation behavior of a novel phenoxy-based thermoplastic and its hybrid FRP, which was investigated by mechanical testing, microscopy, and UV-vis/IR spectroscopy. As part of the analysis of experimental data, some phenomenological life estimation models for both the resin and composite rod are proposed.

2. Experimental procedure

2.1 Material

The polymer in this study was a novel amorphous thermoplastic phenoxy resin developed by Nagase Chemtex. Based on the manufacturer's publications [43-45], aromatic monomers based on bisphenol A and fluorene-bisphenol constitute the main structure of the resin; however, the exact composition is not disclosed. To briefly

describe the production method, the monomer mixture (XNR6850V, aromatic bisphenol and diglycidyl ether compounds) and accelerator (XNH6850V, tertiary amine-based) were mixed at a mass ratio of 100:6.5 and suspended in MEK until ready for use, where it is then heated to 150 °C to promote polymerization and remove solvent [36]. Some scattered crosslinking may occur, but the manufacturer reports no measurable degree of crosslinking [36,43]. Neat resin plates of 2.3-mm thickness (specific gravity 1.20 g/cm^3, provided by the cable manufacturer, Komatsu Matere Co., Ltd.) were cut into 60 × 10 mm rectangular specimens. The hybrid composite rod was comprised of a PAN-based carbon fiber core (Toray T700SC, 24K tow) and a braided E-glass fiber outer sheath (ECG751/01ZY-95T, Nippon Glass Co., Ltd.), which was impregnated with the thermoplastic epoxy during the heating process mentioned above. The composite rod product “NH2417” was selected for this study (labeled “1P” in previous studies [36-42]), obtained from Komatsu Matere Co., Ltd., having a diameter of 2.30 mm and specific gravity of 1.76 g/cm^3, and fiber volume contents of V_{cf} = 24.6% and V_{gf} = 39.8% for carbon fiber and glass fiber, respectively. The thermoplastic resin and hybrid rods are pictured in Figure 1(b)-(d). This small-diameter rod has the lowest carbon fiber content of all CABKOMA products, making it the weakest and most vulnerable to environmental degradation; thus, it was chosen to assess the UV resistance of hybrid

FRP cables through a “weakest link” approach. However, larger sizes are currently under long-term investigation and the results will be reported elsewhere in the future.

Some residual MEK is assumed to remain after the resin manufacturing process, which was confirmed by drying the as-received material in a vacuum oven at 80 °C for two weeks and observing approximately 1% mass loss. The purpose of this study is not to investigate the fundamental photo-oxidation mechanisms of phenoxy-based resin using solvent-free specimens, but rather to assess the real UV durability performance of commercially-available FRP cables for applications that include outdoor exposure, such as seismic retrofitting. Therefore, specimens were used as-received unless specified.

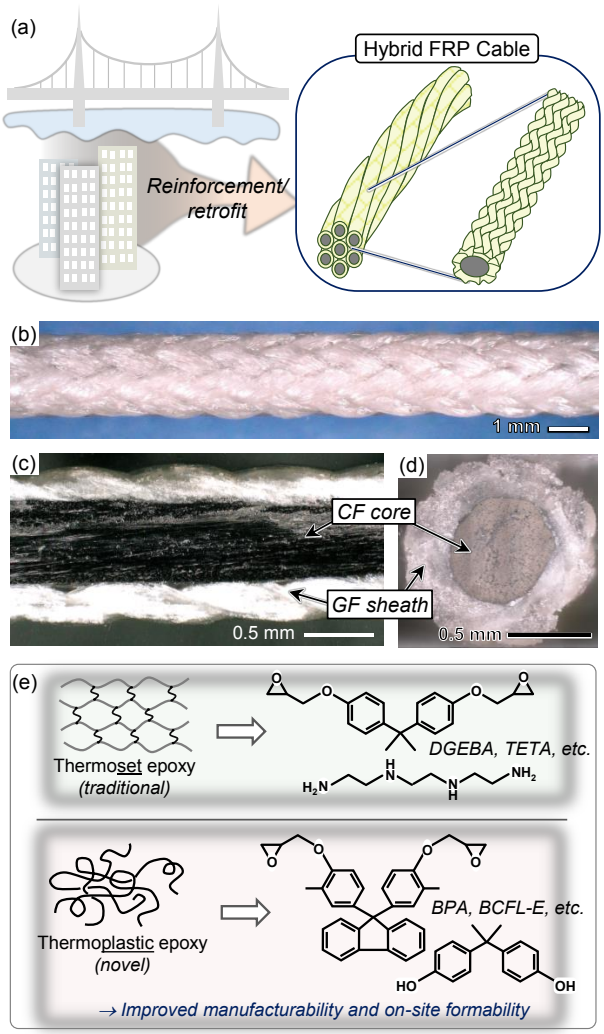

Figure 1. Materials used in this study: (a) Schematic of lightweight hybrid FRP cable for structural reinforcing and retrofit, (b) outer and (c,d) cross-sectional view of the hybrid glass/carbon FRP rod, and (e) diagram of thermoplastic epoxy resin.

2.2 UV exposure conditions

The accelerated weathering test machine used in this study was a xenon arc lamp (SX75, Suga Test Instruments Co. Ltd.), shown in Figure 2. A combination of quartz glass and longpass filters cut wavelengths below 295 nm, with a maximum irradiance of

180 W/m^2 (monitored over 300-400 nm. Temperature and relative humidity constant were kept constant at 37 °C and 50%, respectively.

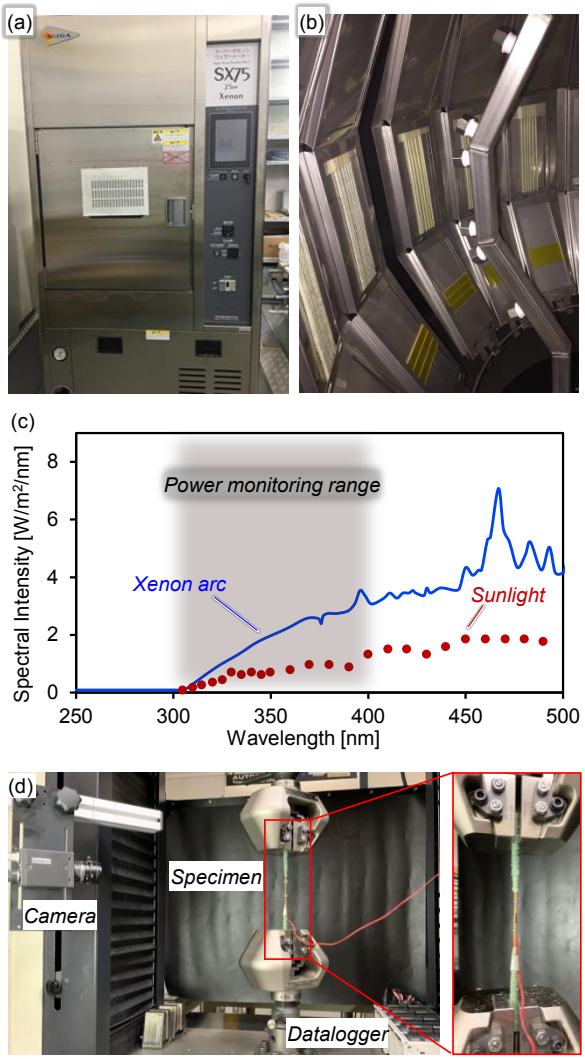

Figure 2. Experimental setup in this study: (a) SX75 xenon arc weathering machine and (b) inside of the SX75 showing specimen fixture, and (c) spectral irradiance of the xenon arc lamp (cut off below 295 nm) according to manufacturer's data; (d) tensile test setup of the hybrid FRP rod.

2.3 Characterization

Chemical changes in the resin were monitored by FTIR spectroscopy (Nicolet 6700,

Thermo Fischer Scientific) over the range 650-4000 cm^{-1} (resolution of 4 cm^{-1} and 300 scans) via Ge-ATR (incident angle 45°, penetration depth ~0.7 μm); specimens were handled with gloves to avoid contamination by skin oils, and spectra were collected from the surface facing the lamp. UV-vis spectra were collected in absorbance mode over the range 200–600 nm (V-770, JASCO). Glass transition temperature (T_g) was measured by differential scanning calorimetry (DSC 7020, Hitachi High-Tech), where 5~6 mg of resin was heated at 10 °C/min over the range of 30–200 °C in a heat-cool-heat program; the T_g was taken from the second heating.

Physical changes were assessed by mass-change measurements using a digital scale (precision ±0.1 mg), and fracture surfaces from the mechanical tests were examined by optical microscope (VHX 6000, Keyence).

Changes in the mechanical properties of the neat resin and hybrid FRP rods were investigated by three-point bending (five replicates) and axial tension (ten replicates), respectively, both at a crosshead speed of 1 mm/min on an electromechanical UTM; tensile strain was measured by a video displacement measurement system and verified by foil strain gauges. A patented hand-layup grip tab technique [36,45] was used to facilitate direct gripping in the UTM. Failure in the center two-thirds of the free length was considered valid.

3. Results and discussion

3.1 Degradation behavior of thermoplastic epoxy

3.1.1 Physical changes

Visible color change was observed after just 300 hours of exposure, growing increasingly yellow as time increased (Figure 3a). This is a common phenomenon associated with oxidation of phenolic substances, as indicated by the absorbance shift to longer wavelengths after exposure [24,30]. The specimen mass decreased over time under the selected exposure conditions, which was calculated by:

$$\Delta M = \frac{W_f - W_i}{W_i} \tag{1}$$

where W_f and W_i are the final and initial weights, respectively. Mass loss with respect to the square root of time showed accelerated loss in early stages followed by a more gradual rate (Figure 3b). This appears to follow the so-called two-stage diffusion model, which describes the combination of molecular diffusion and polymer relaxation-controlled mass transport [14]. We modify this model to enforce equilibrium on the relaxation at long durations:

$$\Delta M = \Delta M_{\infty,1}\left[1 - \exp\left(-7.3\left(\frac{Dt}{h^2}\right)^{0.75}\right)\right] + \Delta M_{\infty,2}(1 - \exp(-kt)) \tag{2}$$

where $\Delta M_{\infty,1}$ is the typical Fickian long-term saturation value, $\Delta M_{\infty,2}$ is the additional change caused by relaxation, k is the relaxation coefficient, t is time, D is the diffusion

coefficient, and h is the material thickness (Table 1). All parameters aside from t and h were determined by minimizing the sum of squared errors against the experimental data. The justification for applying this model—aside from the obvious visual fit—is as follows. Solvent desorption initially follows Fickian behavior due to the small molecular size, and some low molecular weight degradation products from the resin leech out from the outer surface in early stages of exposure; this change in mass is linear vs $\sqrt{t}$ until a certain point ($\Delta M_{\infty,1}$), where a second process seems to dominate. Similar observations have been reported for epoxy adhesives [46]. As the polymer becomes increasingly damaged by UV radiation, leeching of the polymer degradation products and solvent from deeper inside the material dominates the mass loss process and occurs more slowly at longer times, eventually reaching a limit ($\Delta M_{\infty,2}$) in the absence of erosive forces. If surface erosion occurs continuously during exposure, the distance to the outer surface for leeching degradation products and solvent becomes smaller and thus $\Delta M_{\infty,1}$ should theoretically approach $\Delta M_{\infty,2}$. Clearly, the values for D and k in the case of vacuum-drying are nearly an order of magnitude higher than those for UV exposure due to the highly temperature-sensitive nature of desorption kinetics. However, the main focus of this figure is to demonstrate that the observed mass loss during UV exposure can be partially attributed to solvent desorption.

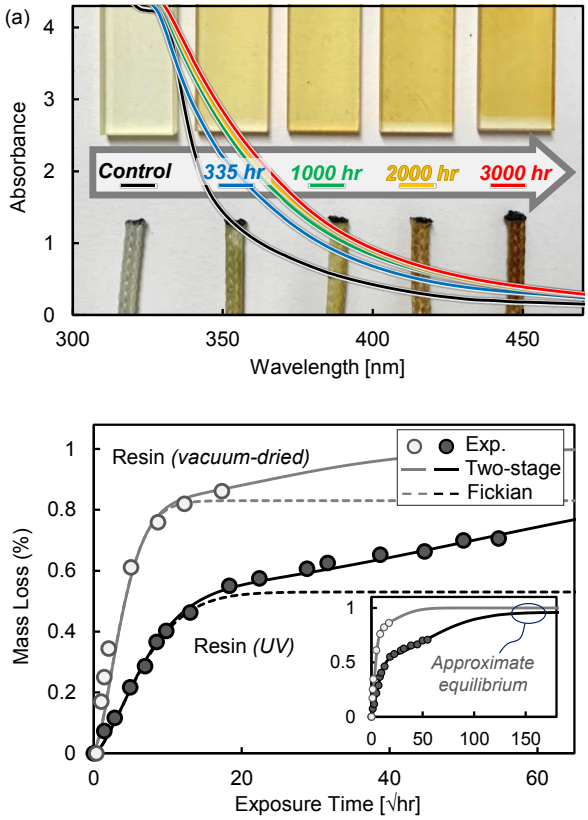

Figure 3. (a) UV-vis spectra and photographs of color change over time, and (b) mass loss of the thermoplastic epoxy resin after UV exposure or vacuum-drying at 80 °C.

Table 1. Parameters for the mass-change model for neat resin.

	UV		Vacuum oven	
	Fickian	Two-stage	Fickian	Two-stage
$\Delta M_{\infty,1}$ (%)	0.53	0.53	0.82	0.82
$\Delta M_{\infty,2}$ (%)	-	0.43	-	0.18
D (10^{-15} m^2/s)	6.1	6.1	19.1	19.1
k (10^{-4} s^{-1})	-	1.9	-	10.3

3.1.2 Mechanical changes

Three-point bending tests show a significant decrease at intermediate durations (<400 hr) followed by a plateau at later stages (>2000), resulting in a strength loss of

88% (Figure 4a). On the other hand, bending modulus increases slightly (16%) at intermediate durations before falling at longer durations (-14%). The initial apparent increase in modulus could be caused by additional crosslinking between polymer chains, as well as the desorption of residual MEK solvent, as supported by the mass-loss results; meanwhile, the loss in strength and overall loss in modulus are attributed to chain scission. Figure 4(b) illustrates the discussion below of the mechanisms behind the modulus behavior. Typical force-displacement curves for bending specimens are shown in Figure 4(c). Two failure modes were observed in degraded specimens, as illustrated in Figure 4(d): (1) multiple small cracks formed along the center-third of the span until one main crack leads to brittle fracture, and (2) a single main crack is immediately formed and the strength is controlled by fracture toughness. There was a roughly equal amount of both failure modes observed, indicating that the crack formation type was random for any given specimen**;** i.e., the strength follows a fracture probability distribution. The fracture surfaces observed by optical microscope (Figure 4e) show brittle fracture with slight ductility in the control specimens, which is expected for a thermoplastic epoxy. By contrast, the degraded specimens exhibit smooth fracture surfaces indicative of micro-crack formation and rapid brittle fracture. This can be expected based on the force-displacement curves.

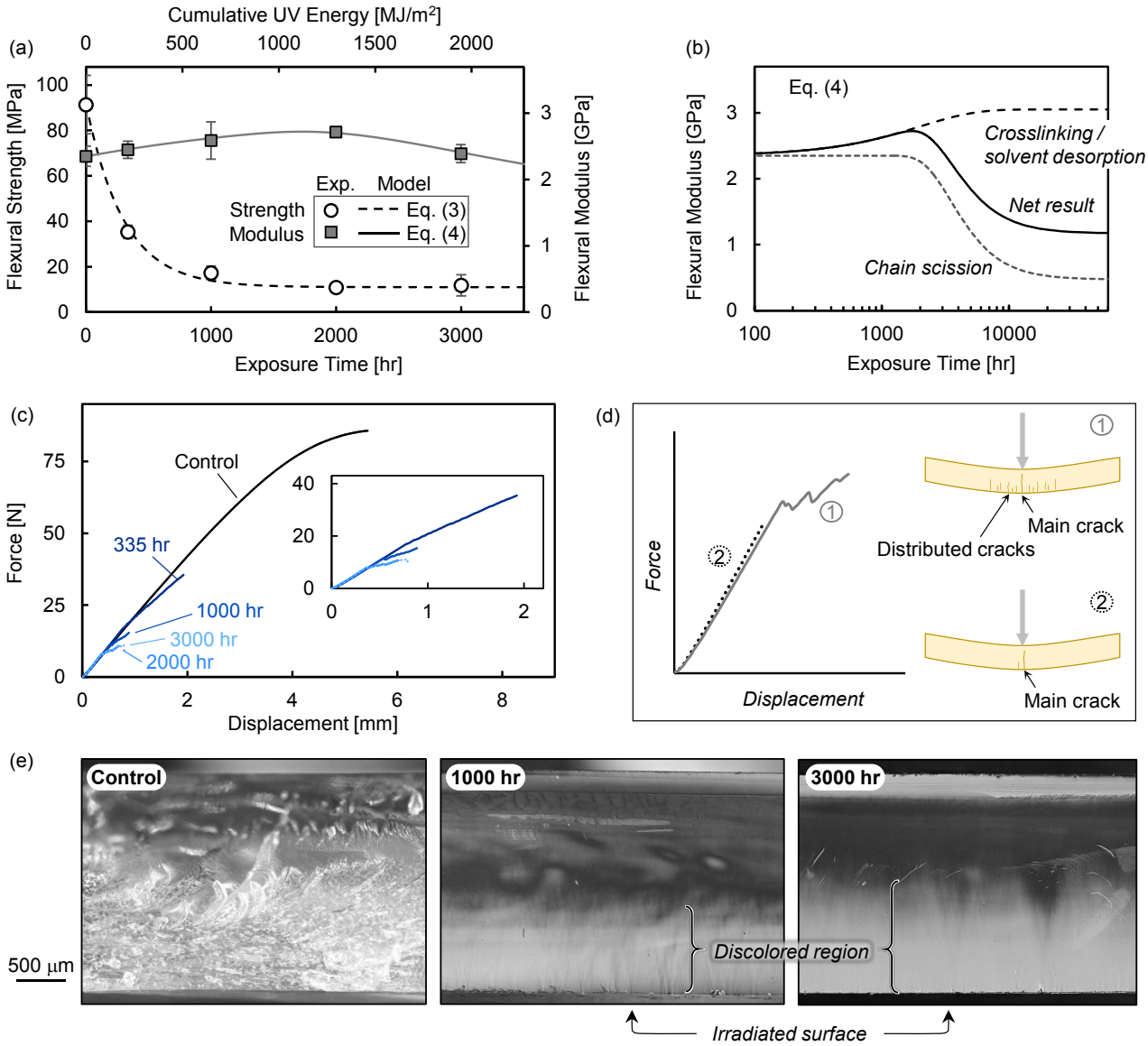

Figure 4. Flexural properties of UV degraded epoxy: (a) flexural strength and modulus over time, (b) partitioned representation of Eq. (5) for modeling flexural modulus, (c) force-displacement curves for different exposure times, (d) schematic of two main failure modes observed, and (e) optical micrographs of fracture surfaces.

Due to the complex nature of concurrent processes in a bulk polymer, it is difficult to experimentally quantify the relationship between mechanical property loss and chain

scission, so we explain the observed behavior as follows. Solvent desorption, crosslinking, and chain scission all occur at a faster rate at short durations—before reaching a plateau—and exhibit a spatial gradient through the thickness; while the former two processes should theoretically increase mechanical properties, the latter should decrease them. Therefore, the relative rates of desorption, crosslinking, and chain scission determine the net resulting mechanical properties at any given time. It follows that since strength largely depends on the development of surface cracks, while modulus is a bulk elastic property, the strength would be more sensitive to chain scission than crosslinking or solvent desorption, whereas the modulus would be the opposite.

Assuming a generic first order reaction process for chain scission, the strength at any time σ_t is expressed as:

$$\sigma_t = (\sigma_0 - \sigma_\infty)\left[1 - \exp\left(-\frac{t}{\tau_1}\right)\right] \quad (3)$$

where σ_0 and σ_∞ denote the values at $t = 0$ and $t \to \infty$, respectively, and τ_1 is a time scaling parameter. The parameters represent the net changes of the scission and crosslinking reactions, reaching some long-term residual strength σ_∞ where the resin degradation rate is too low to be significant on the experimental time scale. Likewise, the bending modulus at any time E_t is a combination of the chain scission and

crosslinking as first order reactions, as well as solve desorption as a near-Fickian process (i.e., exponential):

$$E_t = (E_0 - E_\infty)\left[1 - \exp\left(-\left(\frac{t}{\tau_2}\right)^{\beta}\right)\right] + E_c^{'}\left[1 - \exp\left(-\frac{t}{\tau_3}\right)\right] \quad (4)$$

where β is the stretch parameter for the so-called stretched exponential function, τ_2 and τ_3 are the time scaling parameters, and $E_c^{'}$ is the maximum modulus increase attributed to crosslinking. The stretch parameter is responsible for modifying the initial rate of exponential decay [12,13], which is mathematically convenient for expressing the observed changes in the modulus (i.e., a process influenced by Fickian behavior). Each term in Eq. (4) is plotted separately in Figure 4(b) to help visualize how the "increase" processes (solvent desorption and crosslinking) and "decrease" process (chain scission) interact. All parameters are listed in Table 2, and the equations were successfully fit to the data in Figure 4(a).

Table 2. Parameters for the resin degradation model.

σ_0	σ_∞	τ_1	E_0	E_∞	$E_c^{'}$	τ_2	τ_3	β
91.9	11.0	305	2350	470	700	2000	3500	-2

3.1.3 Chemical changes

FTIR spectra for various exposure times are shown in Figure 5(a), normalized to the

benzene breathing peak at 1508 cm^{-1}. The characteristic benzene stretch peak is found at 1508 and 1605 cm^{-1}, while aromatic ether appears at 1040 and 1240 cm^{-1} and the less-abundant aliphatic ether at 1182 cm^{-1} [23]. Methyl groups from substituted benzene and bisphenol-A units can be seen at 1365 and 1382 cm^{-1}, with several alkyl CH_2 peaks hidden amid other peaks around 1400-1470 cm^{-1}. In the degraded specimens, carbonyl peaks grow with time at 1740 and 1710 cm^{-1}, which could indicate ketone, aldehyde, ester, or carboxylic acid formation; however, no peak at 2700 cm^{-1} indicates aldehyde is not present in significant quantity, and the observed C=O peaks are at a lower wavenumber range than esters typically are found, so ketone and carboxylic acid are the two most likely products [30]. The increase in carbonyl groups follows a linear trend over time (Figure 5c), and does not reach plateau within the duration of the study, in contrast to the bending strength.

Meanwhile, the T_g decreases very slightly (~5 °C) and is assumed to be the net result of concurrent crosslinking, solvent desorption, and chain scission (Figure 5c), which corresponds to the FTIR analyses and mechanical testing results. Equation (5) is analogous to Eq. (4) and was used to fit the T_g data:

$$T_g = \left(T_{g0} - T_{g\infty}\right)\left[1 - \exp\left(-\left(\frac{t}{\tau_2}\right)^{\beta}\right)\right] + T_{gc}^{'}\left[1 - \exp\left(-\frac{t}{\tau_3}\right)\right] \quad (5)$$

where all parameters are analogous to those for elastic modulus in Eq. (4), adapted

to the T_g (listed in Table 3). This demonstrates that the same principle of a net decrease is observed if crosslinking, solvent desorption, and chain scission occur concurrently.

Table 3. Parameters for the T_g reduction model.

T_{g0}	$T_{g\infty}$	$T_{gc}^{'}$	τ_1	τ_2	β
95.3	87.9	97.3	1200	600	1

In order to confirm that a degradation layer is formed rather than uniform degradation through the thickness, a moderately degraded specimen (1000 hr) was selected and the outer surface was polished off in 25 μm increments, and the FTIR spectra were taken again (Figure 5b). Comparing the degraded outer surface (i.e., 0 μm removed) with depths up to 100 μm from the surface, it is clear that the carbonyl and ether peaks decrease significantly and suddenly within 25 m of the surface, as shown in Figure 5(d), and that the inner portion—while no longer virgin—is considerably less degraded and more similar to the initial condition.

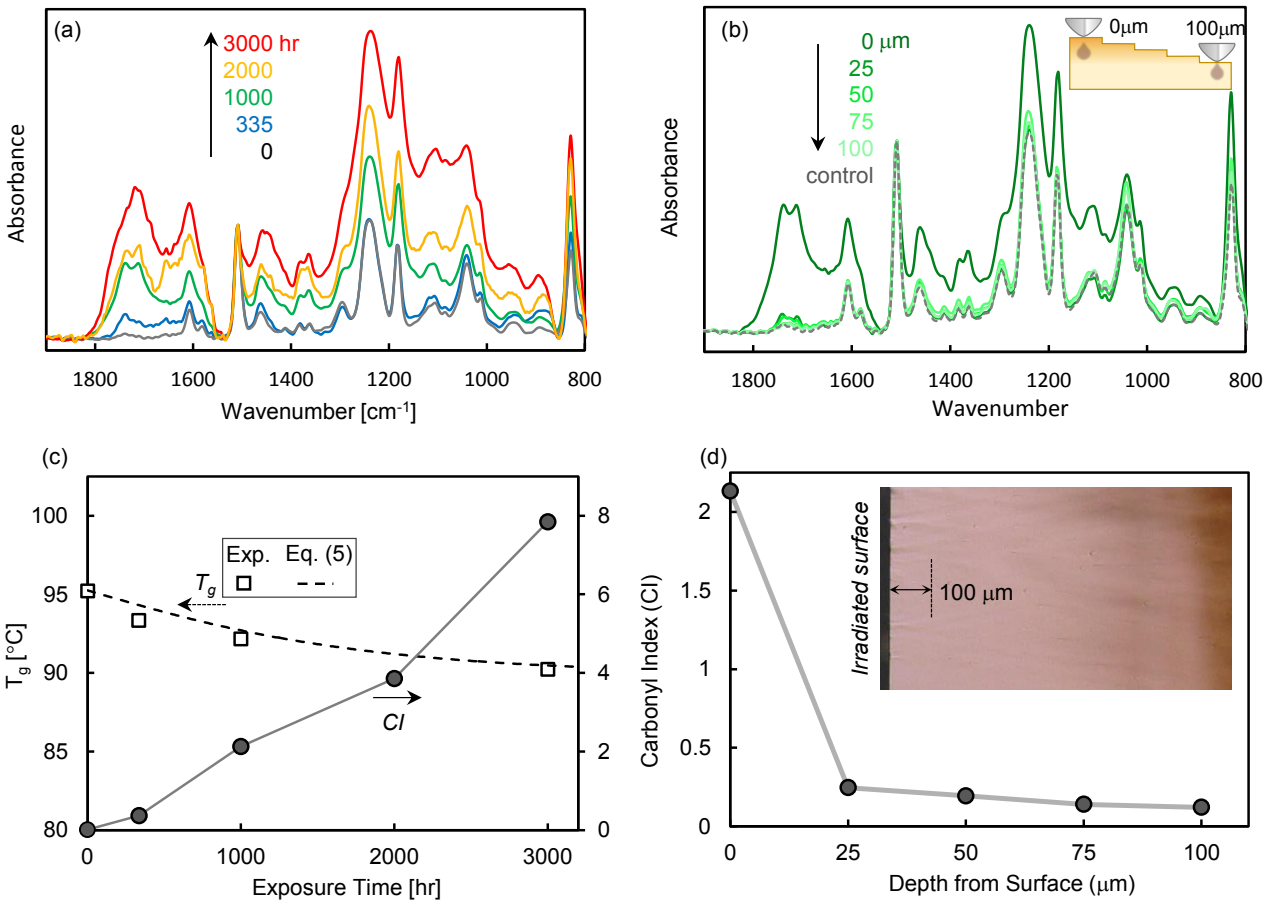

Figure 5. FTIR spectra at (a) various exposure times and (b) different depths from the outer surface (1000 hr specimen), (c) changes in CI and T_g over time, and (d) change in CI through the thickness from (b).

3.2 UV resistance of hybrid FRP

The tensile behavior of the hybrid FRP rods after UV exposure was investigated, revealing linear elastic behavior up to failure for all specimens, which is expected for fiber-dominant tensile properties (Figure 6a). The scatter in tensile strength can be described by the two-parameter Weibull distribution [47]:

$$\ln\left[\ln\left(\frac{1}{1-P_F}\right)\right] = m[\ln(\sigma_u) - \ln(\sigma_m)] \quad (6)$$

where P_F is the cumulative probability of failure at the applied tensile stress σ_u, m is the Weibull modulus or Weibull shape parameter, and σ_m is the characteristic stress or Weibull scale parameter. The higher the value of m, the less scatter in strength is observed and thus the reliability can be considered higher—i.e., lower probability of fracture at strengths approaching the mean. The Weibull plots for all exposure durations are shown in Figure 6(b), where it appears that the data sets differ little from each other.

The tensile strength and modulus, summarized in Figures 6(c)-(e), do not change significantly even after 3000 hours of UV exposure; this is in stark contrast to the neat resin, which lost its mechanical strength at short durations and quickly reached a plateau at long durations. This result is expected as the tensile properties of unidirectional composites are fiber-dominant. To further demonstrate this, we calculated the hybrid FRP tensile properties using a modified Curtin-style global load sharing (GLS) model [42]:

$$\sigma_C = V_{cf}\sigma_{cf}\left(\frac{2}{m_{cf}+2}\right)^{\frac{1}{m_{cf}+1}}\left(\frac{m_{cf}+1}{m_{cf}+2}\right) + \theta_{gf}V_{gf}\sigma_{gf}\left(\frac{2}{m_{gf}+2}\right)^{\frac{1}{m_{gf}+1}}\left(\frac{m_{gf}+1}{m_{gf}+2}\right) + V_m\sigma_m \quad (7)$$

$$\varepsilon_C = \frac{\sigma_{cf}}{E_{cf}}\left(\frac{2}{m_{cf}+2}\right)^{\frac{1}{m_{cf}+1}} + \theta_{gf}\frac{\sigma_{gf}}{E_{gf}}\left(\frac{2}{m_{gf}+2}\right)^{\frac{1}{m_{gf}+1}} \quad (8)$$

$$E_C = \frac{\sigma_C}{\varepsilon_C} \quad (9)$$

where σ, E, and ε are the tensile strength, elastic modulus, and failure strain, respectively; subscripts *cf*, *gf*, and *m* denote the carbon fiber, glass fiber, and matrix, respectively, with respective volume fractions V. The Weibull modulus of each fiber type is denoted by m, and θ is the braiding angle of the glass fiber outer sheath. The fiber properties were taken from the manufacturer, while the respective Weibull moduli and other parameters can be found in the literature and are listed in Table 4 [42]. The resin properties discussed in Section 3.1.2 can be used as direct inputs for material property prediction. The solid lines in Figures 6(c,d) represent model predictions, which agree closely with experimental values. While the predicted strength decreases slightly due to the resin strength degradation, the experimental strength values of the FRP seem to increase very slightly—although within the range of error. Possible mechanisms of strengthening include UV-induced resin crosslinking, improved interfacial bonding due to UV-induced carboxylation, or solvent desorption (as discussed in Section 3.1).

Table 4. Parameters for the GLS model of FRP properties [42].

	Carbon fiber	Glass fiber	Resin
V (%)	24.6	39.8	~25.5
E (GPa)	230	70	2.3
σ (MPa)	4900	2200	12~90*

m (-)	6.0	5.5	-
θ (deg)	-	9.12	-

Resin strength varies according to Eq. (3)

The Weibull modulus increases initially and then decreases linearly with exposure time (Figure 6e), resulting in a 37.4% maximum reduction. Although the mean tensile strength does not change significantly over the duration of this study, the scatter in strength becomes greater after UV exposure and thus the risk of material failure at lower applied stresses increases. This warrants further investigation into much longer exposure durations to determine whether accelerated UV testing can provide data for life prediction at reasonable time scales—which is currently in progress.

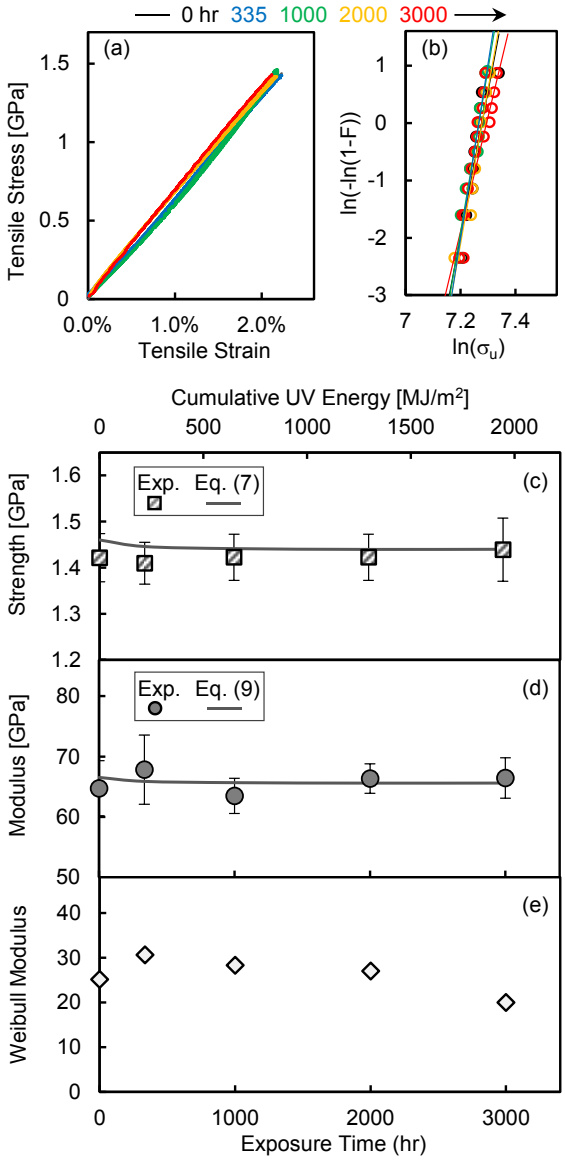

Figure 6. Tensile properties of hybrid FRP rods after UV exposure: (a) Representative stress-strain curves and (b) Weibull plot of tensile strength for each exposure duration; (c) tensile strength, (d) elastic modulus, and (e) Weibull modulus at different exposure times.

Figure 7 shows the fracture surfaces of the rods at different exposure durations. A distinct trend was observed in which the resin matrix degradation leads to “unraveling”

of the braided glass sheath, appearing almost as a broom-like failure at longer exposure times. In addition, the carbon fiber core appears to exhibit more brittle fracture with debris-like resin fragments visible after UV exposure. Both of these observations could suggest that the resin degradation has a small effect on the local fracture behavior in the hybrid composite, although this is not reflected in the average tensile properties.

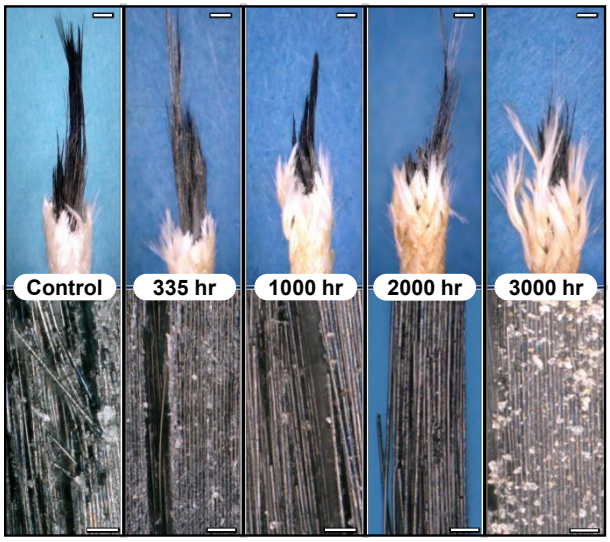

Figure 7. Fracture surface of hybrid FRP after different UV exposure times (scale bars are 1 mm and 50 μm for top and bottom, respectively).

The results presented in this paper are limited to the center rod of the CABKOMA stranded cable product having the smallest diameter, in order to rapidly assess the worst case in terms of UV resistance. If a single rod from the stranded cable does not show significant degradation, then the full seven-wire stranded cable should be even more durable due to the smaller exposed surface area, which can be approximated as roughly

40% of the total surface area of seven individual rods (Figure 8). Thus, the neat thermoplastic epoxy resin and the NH2417 ("1P") rod were sufficient as model materials to study the effects of UV radiation on mechanical properties. However, a long-term study on UV exposure of larger diameter rods (NH2437, "3P") and full stranded cables simulating 100 years of outdoor exposure is in-progress, and the results will be reported in the future.

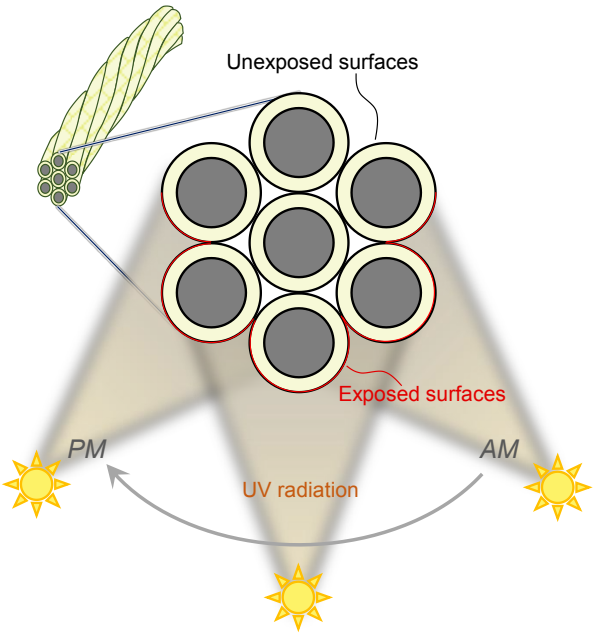

Figure 8. Schematic depiction of exposed surfaces in a full seven-wire stranded cable.

4. Conclusions

This paper presents an investigation into the accelerated UV degradation behavior of a novel phenoxy-based thermoplastic epoxy resin, as well as the corresponding hybrid glass/carbon FRP rod. A maximum strength loss of 88% was observed within 3000

hours of accelerated testing of the resin, which is equivalent to sunlight exposure of 6.94 years in Florida, USA (based on total irradiance of 1944 MJ/m^2, and annual UV dose of 280 MJ/m^2 in Florida [48]). Although this would hypothetically translate to significantly compromised mechanical integrity of the FRP in the long term, tensile testing of the rods showed no significant changes in tensile properties even after 3000 hours of UV exposure. The UV resistance of the rods are attributed to the unidirectional structure consisting of a glass fiber outer sheath, so that the fiber-dominant properties are maintained despite degradation of the outer layer of resin. FRP rods used as internal reinforcement (i.e., embedded in concrete) are generally safe from UV radiation, but cables used as external rehabilitation or seismic retrofitting materials are at high risk of UV exposure, so this study provides valuable information on the performance of a novel thermoplastic epoxy-based hybrid FRP cable for construction applications. Ongoing and future studies will investigate the UV resistance of larger diameter rods and cables, as well as coupled effects of UV and moisture.

Acknowledgements

This research was promoted by COI program "Construction of next-generation infrastructure using innovative materials ～Realization of safe and secure society that

can coexist with the Earth for centuries～" supported by Japan Science and Technology Agency (JST).

Conflict of interests

The authors declare that they have no conflict of interest.

References

1. Koch G, Brongers M, Thompson N, Virmani Y, Payer J. Corrosion costs and preventative strategies in the United States. Federal Highway Administration Report FHWA-RD-01-156 (2003).

2. Val DV, Stewart MG. Life-cycle cost analysis of reinforced concrete structures in marine environments. Struct Saf 2003:25:343-362.

3. Cheung MMS, So KKL, Zhang X. Life cycle cost management of concrete structures relative to chloride-induced reinforcement corrosion. Struct Infrastruct Eng 2012:8:1136-1150.

4. Zdanowicz K, Kotynia R, Marx S. Prestressing concrete members with fibre-reinforced polymer reinforcement: State of research, Struct Concr 2019:20:872-885.

5. Balaguru P, Nanni A, Giancaspro J. FRP composites for reinforced and prestressed concrete structures: a guide to fundamentals and design for repair and retrofit. New York: Taylor, 2009.

6. Meier U. Composite materials in bridge repair. Appl Compos Mater 2000:7:75-94.

7. Maissen A. Concrete beams prestressed with CFRP strands. Struct Eng Int 1997:7:284-287.

8. Meier U. Carbon fiber reinforced polymer cables: Why? Why Not? What If? Arab J Sci Eng 2012:37:399-411.

9. Komatsu Matere Co., Ltd., *CABKOMA*, retrieved from:

https://www.komatsumatere.co.jp/cabkoma/en/

10. Hollaway LC. Key issues in the use of fibre reinforced polymer (FRP) composites in the rehabilitation and retrofitting of concrete structures. In: Karbhari VM, Lee LS, editors. Service Life Estimation and Extension of Civil Engineering Structures. Cambridge: Woodhead Publishing, 2011. p. 3.

11. Tanks JD, Kubouchi M, Arao Y. Influence of network structure on the degr11.adation of poly(ether)amine-cured epoxy resins by inorganic acid. Polym Degrad Stabil 2018:157:153-159.

12. Tanks JD, Kubouchi M, Arao Y. Diffusion kinetics, swelling, and degradation of corrosion-resistant C-glass/epoxy woven composites in harsh environments. Compos Struct 2018:202:686-694.

13. Tanks JD, Sharp SR, Harris DK. Kinetics of in-plane shear degradation in carbon/epoxy rods from exposure to alkaline and saline environments. Compos Part B 2017:110:204-212.

14. Tanks JD, Sharp SR, Harris DK, Ozyildirim C. Durability of CFRP cables exposed to simulated concrete environments. Adv Compos Mater 2017:26:245-258.

15. Duo Y, Liu X, Liu Y, Tafsirojjaman T, Sabbrojjaman M. Environmental impact on the durability of FRP reinforcing bars. J Build Eng 2021:43:102909.

16. Hassan MA, Usman M, Hanif A, Farooq SH, Ahmed J. Improving structural performance of timber wall panels by inexpensive FRP retrofitting techniques. J Build Eng 2020:27:101004.

17. Radhi MS, Hassan MS, Gorgis IN. Carbon fibre-reinforced polymer confinement of corroded circular concrete columns. J Build Eng 2021:43:102611.

18. Cavdar AD, Tomak ED, Torun SB, Arpaci SS. Accelerated weathering resistance of high-density polyethylene composites reinforced with microcrystalline cellulose and fire retardants. J Build Eng 2021:39:102282.

19. Awad SA, Fellows CM, Mahini SS. A comparative study of accelerated weathering of epoxy resins based on DGEBA and HDGEBA. J Polym Res 2018:25:103.

20. Rivaton A, Mailhot B, Soulestin J, Varghese H, Gardette JL. Comparision of the photochemical and thermal degradation of bisphenol-A polycarbonate and trimethylcyclohexane-polycarbonate. Polym Degrad Stabil 2002:75:17-33.

21. Cysne Barbosa AP, Fulco APP, Guerra ESS, Arakaki FK, Tosatto M, Costa MCB, Melo JDD. Accelerated aging effects on carbon fiber/epoxy composites. Compos Part B 2017:110:298-306.

22. Bajracharya RM, Manalo AC, Karunasena W, Lau K. Durability characteristics and property prediction of glass fibre reinforced mixed plastics composites, Compos Part B 2017:116:16-29.

23. He Y, Suliga A, Brinkmeyer A, Schenk M, Hamerton I. Atomic oxygen degradation mechanisms of epoxy composites for space applications. Polym Degrad Stabil 2019:166:108-120.

24. Nikafshar S, Zabihi O, Ahmadi M, Mirmohseni A, Taseidifar M, Naebe M. The effects of UV light on the chemical and mechanical properties of a transparent epoxy-diamine system in the presence of an organic UV absorber. Materials 2017:10:180.

25. Bazli M, Jafari A, Ashrafi H, Zhao X-L, Bai Y, Raman RKS. Effects of UV radiation, moisture and elevated temperature on mechanical properties of GFRP pultruded profiles. Constr Build Mater 2020:231:117137.

26. Bazli M, Zhao X-L, Jafari A, Ashrafi H, Bai Y, Raman S, Khezrzadeh H. Mechanical properties of pultruded GFRP profiles under seawater and concrete environment coupled with UV radiation and moisture. Constr Build Mater 2020:258:120369.

27. Chennareddy R, Tuwair H, Kandil UF, ElGawady M, Reda Taha MM. UV-resistant GFRP using carbon nanotubes. Constr Build Mater 2019:220:679-689.

28. Rivaton A, Moreau L, Gardette JL. Photo-oxidation of phenoxy resins at long and short wavelengths—I. Identification of the photoproducts. Polym Degrad Stabil 1997:58:321-332.

29. Rivaton A, Moreau L, Gardette JL. Photo-oxidation of phenoxy resins at long and short wavelengths—II. Mechanisms of formation of photoproducts. Polym Degrad Stabil 1997:58:333-339.

30. Malajati Y, Therias S, Gardette JL. Influence of water on the photo-oxidation of KHJ® phenoxy resins, 1. Mechanisms. Polym Degrad Stabil 2011:96:144-150.

31. Larche JF, Bussiere PO, Therias S, Gardette JL. Photooxidation of polymers: Relating material properties to chemical changes. Polym Degrad Stabil 2012:97:25-34.

32. Yousif E, Haddad R. Photodegradation and photostabilization of polymers, especially styrene: review. SpringerPlus 2013:2:398.

33. Musto P, Ragosta G, Abbate M, Scarinzi G. Photo-oxidation of high performance epoxy networks: Correlation between the molecular mechanisms of degradation and the viscoelastic and mechanical response. Macromol. 2008:41:5729-5743.

34. Gewert B, Plassmann MM, Macleod M. Pathways for degradation of plastic polymers floating in the marine environment. Environ Sci: Process Impacts

2015:17:1513-1521.

35. Yu Y, Xu P, Chang M, Chang J. Aging properties of phenol-formaldehyde resin modified by bio-oil using UV weathering. Polymers 2018:10:1183.

36. Naito K, Oguma H. Tensile properties of novel carbon/glass hybrid thermoplastic composite rods. Compos Struct 2017:161:23-31.

37. Naito K, Oguma H. Tensile properties of novel carbon/glass hybrid thermoplastic composite rods under static and fatigue loading. Revista Materia 2017:22:11843.

38. Naito K, Nagai C, Tanaka Y. Transverse compressive properties of carbon/glass hybrid thermoplastic composite rods. J Phys Sci Appl 2019:9:25-33.

39. Naito K, Nagai C. Axial compressive properties of carbon/glass thermoplastic epoxy hybrid composite rods. J Mater Eng Perform 2020:29:4804-4813.

40. Naito K. Interfacial mechanical properties of carbon/glass hybrid thermoplastic epoxy composite rods. Compos Struct 2021:257:113129.

41. Naito K. Flexural properties of carbon/glass hybrid thermoplastic epoxy composite rods under static and fatigue loadings. Appl Compos Mater 2021:28:753-766.

42. Naito K, Oguma H, Nagai C. Temperature-dependent tensile properties of hybrid carbon-glass thermoplastic composite rods. Polym Compos 2020:41:3985-3995.

43. Nagase ChemteX Corporation. Process for Production of Thermoplastic Cured Epoxy Resin with Transparency to Visible Light, and Thermoplastic Epoxy Resin Composition. United States Patent Application Publication, Pub. No. US 2014/0194590 A1. 2014.

44. Imanishi T, Nishida H, Hirayama N, Tomomitsu N. In-situ polymerizable thermoplastic epoxy resin and high performance FRTP using it and fiber fabrics, *16th International Conference on Composite Materials*, Kyoto, Japan, 8-13 July, 2007.

45. Komatsu Matere Co., Ltd., and National Institute for Materials Science (NIMS). Attachment Structure for Fiber Reinforced Plastic Cable, Manufacturing Method for Same, Strength Test Method, and Sample for Strength Test. Japan Patent Office, JP 6586695 B2. 2019. (in Japanese)

46. Machado JJM, Marques EAS, Barbosa AQ, da Silva JFM. Effect of hygrothermal aging on the quasi-static behavior of CFRP joints varying the overlap length. Compos Struct 2019:214:451-462.

47. Weibull W. A statistical distribution function of wide applicability. J Appl Mech 1951:18:293-297.

48. Erdmann M, Kleinbub S, Wachtendorf V, Schuter JD, Niebergall U, Böhning M, Koerdt A. Photo-oxidation of PE-HD affecting polymer/fuel interaction and bacterial attachment. npj Mater Degrad 2020:4:18.